Structural foundations of optogenetics: Determinants of channelrhodopsin ion selectivity

Andre Berndt[a,1], Soo Yeun Lee[a,1], Jonas Wietek[b,1], Charu Ramakrishnan[a], Elizabeth E. Steinberg[c,d], Asim J. Rashid[e], Hoseok Kim[f], Sungmo Park[e], Adam Santoro[e], Paul W. Frankland[e], Shrivats M. Iyer[a], Sally Pak[a], Sofie Ährlund-Richter[f], Scott L. Delp[a], Robert C. Malenka[c,d], Sheena A. Josselyn[e], Marie Carlén[f], Peter Hegemann[b], and Karl Deisseroth[a,c,g,2]

[a]Department of Bioengineering, Stanford University, Stanford, CA 94305; [b]Institute for Biology, Experimental Biophysics, Humboldt Universität zu Berlin, D-10115 Berlin, Germany; [c]Department of Psychiatry and Behavioral Sciences, Stanford University, Stanford, CA 94305; [d]Nancy Pritzker Laboratory, Stanford University, Stanford, CA 94305; [e]Program in Neurosciences and Mental Health, Hospital for Sick Children, University of Toronto, Toronto, ON, Canada M5G 1X8; [f]Department of Neuroscience, Karolinska Institutet, SE-171 77 Stockholm, Sweden; and [g]Howard Hughes Medical Institute, Stanford University, Stanford, CA 94305

This contribution is part of the special series of Inaugural Articles by members of the National Academy of Sciences elected in 2012.

Contributed by Karl Deisseroth, November 30, 2015 (sent for review November 16, 2015; reviewed by Lily Yeh Jan and Anatol Kreitzer)

The structure-guided design of chloride-conducting channelrhodopsins has illuminated mechanisms underlying ion selectivity of this remarkable family of light-activated ion channels. The first generation of chloride-conducting channelrhodopsins, guided in part by development of a structure-informed electrostatic model for pore selectivity, included both the introduction of amino acids with positively charged side chains into the ion conduction pathway and the removal of residues hypothesized to support negatively charged binding sites for cations. Engineered channels indeed became chloride selective, reversing near −65 mV and enabling a new kind of optogenetic inhibition; however, these first-generation chloride-conducting channels displayed small photocurrents and were not tested for optogenetic inhibition of behavior. Here we report the validation and further development of the channelrhodopsin pore model via crystal structure-guided engineering of next-generation light-activated chloride channels (iC++) and a bistable variant (SwiChR++) with net photocurrents increased more than 15-fold under physiological conditions, reversal potential further decreased by another ∼15 mV, inhibition of spiking faithfully tracking chloride gradients and intrinsic cell properties, strong expression in vivo, and the initial microbial opsin channel-inhibitor–based control of freely moving behavior. We further show that inhibition by light-gated chloride channels is mediated mainly by shunting effects, which exert optogenetic control much more efficiently than the hyperpolarization induced by light-activated chloride pumps. The design and functional features of these next-generation chloride-conducting channelrhodopsins provide both chronic and acute timescale tools for reversible optogenetic inhibition, confirm fundamental predictions of the ion selectivity model, and further elucidate electrostatic and steric structure–function relationships of the light-gated pore.

optogenetics | channelrhodopsin | structure | chloride | neuronal inhibition

Discovery and engineering of the microbial opsin genes not only has stimulated basic science investigation into the structure–function relationships of proteins involved in light-triggered ion flow but also has opened up opportunities for biological investigation (reviewed in ref. 1) via the technique of optogenetics, which involves targeting these genes and corresponding optical stimuli to control activity within specified types of cells within intact and functioning biological systems. For example, optogenetics has been used to identify causally the brain cells and projections involved in behaviors relevant to memory formation, affective states, and motor function, among many other discoveries (2–4). For the channelrhodopsins, an important member of this protein family widely used in optogenetics (5, 6), the light-activated cation-conducting channel pore has been the subject of structural investigation, both because of curiosity regarding the physical properties of its ion conduction and because the creation of inhibitory channels had been sought for optogenetic applications. Converging lines of work recently achieved the latter goal; resolving the high-resolution structure of channelrhodopsin (7) allowed a principled structure-guided approach to engineering for chloride selectivity by testing an electrostatic model for pore function (8, 9). Subsequently, by screening the genome of the *Guillardia theta* microbe, two naturally occurring light-gated chloride-conducting channelrhodopsins (10) were identified.

Because optogenetic control of behavior has not yet been demonstrated with chloride channelrhodopsins, and to test further integrative ideas regarding pore function from structural considerations as shown here, we sought to design and test the next generation of enhanced chloride channels (iC++ and SwiChR++). Along the way, we provide the initial test of the hypothesis that light-activated channels will be more efficient tools than pumps for optogenetic neuronal inhibition at the cellular level, demonstrate the initial utility of light-gated chloride channels in controlling behavior in freely moving animals, and reveal key principles regarding the functional selectivity of light-gated ion channel pores.

Significance

Channelrhodopsins are membrane proteins that enable cellular regulation of transmembrane ion conductance through light-gated pores; these proteins have found application in optogenetics. This paper tests the hypothesis that selectivity of channelrhodopsins is determined by surface potential of the pore region: Cations are conducted by a negatively charged pore, and chloride ions are conducted by a pore that has neutral and positively charged residues. In confirming this hypothesis and applying the resulting principles, we engineer improved chloride-conducting channels with higher chloride selectivity and conductivity. We also provide insights into the distinct mechanisms underlying inhibition mediated by higher-efficiency chloride channels compared with ion pumps. Finally, we demonstrate initial utility of light-gated microbial opsin-based chloride channels in controlling behavior of freely moving animals.

Author contributions: A.B., S.Y.L., and K.D. designed the project; A.B., S.Y.L., J.W., C.R., E.E.S., A.J.R., H.K., S. Park, A.S., S.M.I., S. Pak, and S.Ä.-R. performed research; C.R. contributed new reagents/analytic tools; A.B., S.Y.L., J.W., E.E.S., A.J.R., H.K., S. Park, A.S., P.W.F., S.M.I., S.Ä.-R., S.L.D., R.C.M., S.A.J., M.C., and P.H. analyzed data; A.B., S.Y.L., and K.D. wrote the paper; and K.D. supervised all aspects of the work.

Reviewers: L.Y.J., University of California, San Francisco; and A.K., University of California, San Francisco.

The authors declare no conflict of interest.

Freely available online through the PNAS open access option.

[1]A.B., S.Y.L., and J.W. contributed equally to this work.

[2]To whom correspondence should be addressed. Email: deissero@stanford.edu.

This article contains supporting information online at www.pnas.org/lookup/suppl/doi:10.1073/pnas.1523341113/-/DCSupplemental.

Results

Structural Determinants of Chloride Selectivity in Channelrhodopsins. Previous work showed that iC1C2 (engineered using a crystal structure-based electrostatic pore model) had higher chloride selectivity and conductivity at lower pH (8). This pH effect was suggested to be caused by protonation within the pore and more positive local electrostatic potential, indicating that it might be possible to enhance chloride flux at physiological pH further by further developing the electrostatic selectivity hypothesis (8). To test this concept, we began by introducing a number of additional point mutations to iC1C2, specifically targeting residues in the ion-conduction pathway to enhance chloride flux guided by our model; reversal potential (V_{rev}) and photocurrent size were tracked for all variants (Fig. 1 *A–D*) in cultured hippocampal neurons using whole-cell patch-clamp recordings.

The largest shift in V_{rev} was seen with E83 mutations, but these also drastically reduced neuronal input resistance (R_{in}) (Fig. 1*C*), as was consistent with creation of a leak current. We observed that E83 is positioned close to R134 in iC1C2, which had been a histidine in the parental C1C2 chimera (Fig. 1 *E* and *F*) and indeed has been conserved as a histidine in both wild-type channelrhodopsins 1 and 2. Because both E83 and R134 were shown to be inner pore-gate residues in the C1C2 structure (7), we considered the possibility that a disruptive interaction had been created here by joint mutation at these two residues. Indeed, the longer arginine side chain (compared with histidine) could, in principle, interfere with channel closure of iC1C2-E83X mutants, increasing leak currents in the dark and leading to reduced R_{in} for these otherwise interesting E83 variants. Therefore we tested reversion of this arginine back to the histidine that is present in wild-type channelrhodopsins; as hypothesized (and as was consistent with our structural model), R134H increased R_{in} and photocurrent size of the iC1C2-E83X mutations. E83N then was carried through to our final construct here along with R134H (Fig. 1 *A–C*).

Next, chloride selectivity was enhanced further with structure-guided pore replacement of two additional lysines by higher-pK_a arginines (K117R and K242R) and replacement of a second negatively charged amino acid of the inner pore exit with a neutral amino acid (E273S, similar in expected electrostatic effect to E83N). Finally, replacement of serine 90 in iC1C2 with glutamine further hyperpolarized the V_{rev}; the final construct (the sequence is shown in *SI Appendix*, Fig. S1) displayed a significantly negatively shifted V_{rev}, larger photocurrent size at the action potential (V_{AP}) threshold, and larger R_{in} compared with iC1C2 (Fig. 1 *A–D*). Because this mutant showed substantially improved properties in all dimensions, we denote the variant

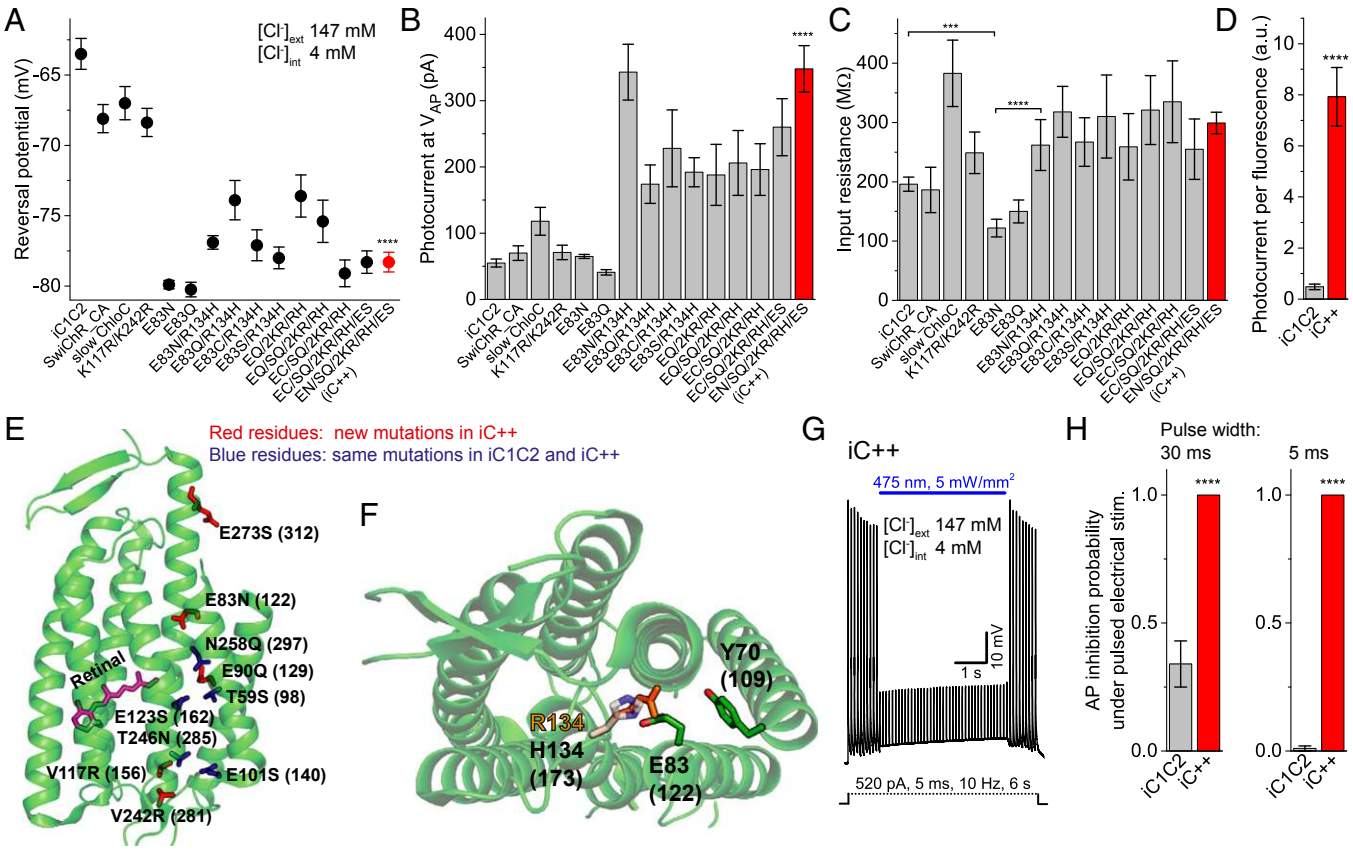

Fig. 1. Design and characterization of iC++ in cultured neurons of rat hippocampus. (*A*) V_{rev} of iC1C2 mutations compared with chloride-conducting channelrhodopsins at an intracellular chloride concentration of 4 mM. EN/Q/C: E83N/Q/C; ES: E273S; RH: R134H; SQ: S90Q; 2KR: K117R/K242R. (*B*) Photocurrent amplitudes measured at the V_{AP} (−51 ± 4 mV). (*C*) R_{in} of channelrhodopsin-expressing cells. (*D*) Stationary photocurrents per fluorescence of eYFP-tagged constructs expressed in cultured neurons. (*E*) C1C2 structure depicting iC++ mutations. Numbering refers to N-terminal–truncated channel iC++. Corresponding positions in the original C1C2 structure are indicated in parentheses. (*F*) Structural model of the putative cytosolic ion gate in C1C2. Histidine 134 (173) (gray) was replaced by arginine in iC1C2 (orange) but not in iC++. (*G*) Voltage trace of a cultured neuron expressing iC++. APs were evoked by pulsed electrical inputs at 10 Hz (dotted line) and were inhibited by continuous light application (blue bar) for 4 s. (*H*) Inhibition probability of APs evoked by pulsed current injections (6 s, 10 Hz) with pulse widths of 30 ms (*Left*), and 5 ms (*Right*) under 4-s light application. Current inputs were individually titrated to the V_{AP}. Shorter pulses required stronger current amplitudes. Average: 30 ms: 202 ± 11 pA; 5 ms: 559 ± 40 pA. pH_{ext} = 7.3, pH_{int} = 7.2; $[Cl^-]_{ext}$ = 147 mM, $[Cl^-]_{int}$ = 4 mM for entire figure. ***$P < 0.005$, ****$P < 0.0001$. Error bars indicate SEM; all values and numbers are listed in *SI Appendix*, Table S1.

here as "iC++" (with the "++" notation both indicating the next increment in the development of inhibitory channelrhodopsins and referencing the expected increase in approximately two positive charges in the pore resulting from the replacement of two additional glutamate residues). Protein expression levels of iC++ were comparable to those of iC1C2 (*SI Appendix*, Fig. S2), but the effective photocurrent size of iC++ was more than 16 times larger (Fig. 1*D*), whereas membrane properties of cells expressing iC++ remained comparable to those of eYFP-expressing cells (*SI Appendix*, Fig. S2).

We next carried out in vitro verification of the capability of iC++ to inhibit electrically evoked action potentials (APs) elicited by current injection. Because the use of continuously varying current ramps can cause confounds from use-dependent alteration in both channelrhodopsin function and neuronal membrane properties, we instead tested different current injection parameters independently, beginning with separate delivery of strong and fast (5-ms) or moderate and slow (30-ms) current injections, in each case titrated to the level needed to drive trains of APs faithfully in the recorded cell. iC++ demonstrated a robust spike inhibition capability, with particular advantages over iC1C2 in the setting of short 5-ms pulse widths where strong current amplitudes of >500 pA were required to induce spiking (Fig. 1 *G* and *H*).

iC1C2 and iC++ are highly engineered (9 and 10 residues were replaced, respectively) variants of the cation-selective parental construct C1C2, with mutations chosen for the predicted ability to alter the electrostatic potential of the ion-conducting pore from predominantly negative to predominantly positive (7, 8, 11). From the crystal structure we had predicted the channelrhodopsin pore to be relatively large, disordered, and without high-affinity ion-binding sites (7, 8, 11); the iC1C2/iC++ engineering was designed accordingly and was predicted to exclude positively charged cations and to conduct negatively charged ions such as chloride (Fig. 2). Interestingly, the newly discovered natural light-gated chloride channel *Gt*ACR2 (10) exhibits finely detailed similarity in predicted pore electrostatics to the iC1C2 and iC++ mutations (Fig. 2), which were generated before knowledge of *Gt*ACR2 and in which specific side chains facing the pore are replaced by less polar or nonpolar residues, just as seen in *Gt*ACR2: for example, *Gt*ACR2-S57 (C1C2/iC++: E122/N83), *Gt*ACR2-A71 (C1C2/iC++: E140/S101), and *Gt*ACR2-S93 (C1C2/iC++: E162/S123) (*SI Appendix*, Fig. S1). This striking convergence reveals that the engineering of iC1C2 and iC++ for chloride conductance based entirely on the structure-derived model of electrostatic pore selectivity (7, 8) resulted in a solution very similar to that arrived at by nature over the long timescales of evolution; the overall model for ion selectivity is consistent in both natural and engineered channelrhodopsins (Fig. 2).

iC++: Chloride Selectivity and pH Dependency. We next probed the biophysical properties of iC++ in HEK293 cells to confirm V_{rev} and chloride dependence in a setting independent of neuronal active conductances. We observed, as expected, outward iC++ currents in the setting of inward-directed chloride gradients ($[Cl^-]_{ext}$ = 150 mM, $[Cl^-]_{int}$ = 10 mM) (Fig. 3*A* and *SI Appendix*, Fig. S2), with an initial peak stabilizing to a stationary current. We systematically measured V_{rev} with varying intracellular chloride concentrations (Fig. 3 *B* and *C*); the V_{rev} of the peak and stationary currents closely matched the expected equilibrium potential under various chloride gradients, indicating the high chloride selectivity of the channel. We also found that iC++-expressing HEK293 cells maintained R_{in} even under strong chloride gradients in the dark; in contrast, iC1C2-expressing cells showed decreased R_{in} in the setting of strongly shifted chloride gradients, indicating that iC1C2, but not iC++, may exhibit slight current in HEK293 cells in the dark under these culture conditions (Fig. 3*D*). The peak activation wavelength of iC++ was measured to be 488 nm (*SI Appendix*, Fig. S2), suggesting that the properties of the retinal-binding pocket environment were maintained.

We previously reported that iC1C2 exhibited a degree of pH dependency, with increased chloride conductivity and selectivity at lower intracellular and lower extracellular pH (8). The newly introduced mutations of iC++ were found here to reduce this pH-dependent increase in photocurrent size, confirming a stable, highly chloride-conducting state in the iC++ pore (Fig. 3 *E* and *F*). Moreover, the V_{rev} of iC++ was independent of the proton gradient, in contrast to iC1C2, indicating that iC++ does not conduct protons (Fig. 3*G*). Additional characterization with ion-substitution experiments revealed that iC++ can conduct other anions, such as iodide and bromide, but not small organic anions

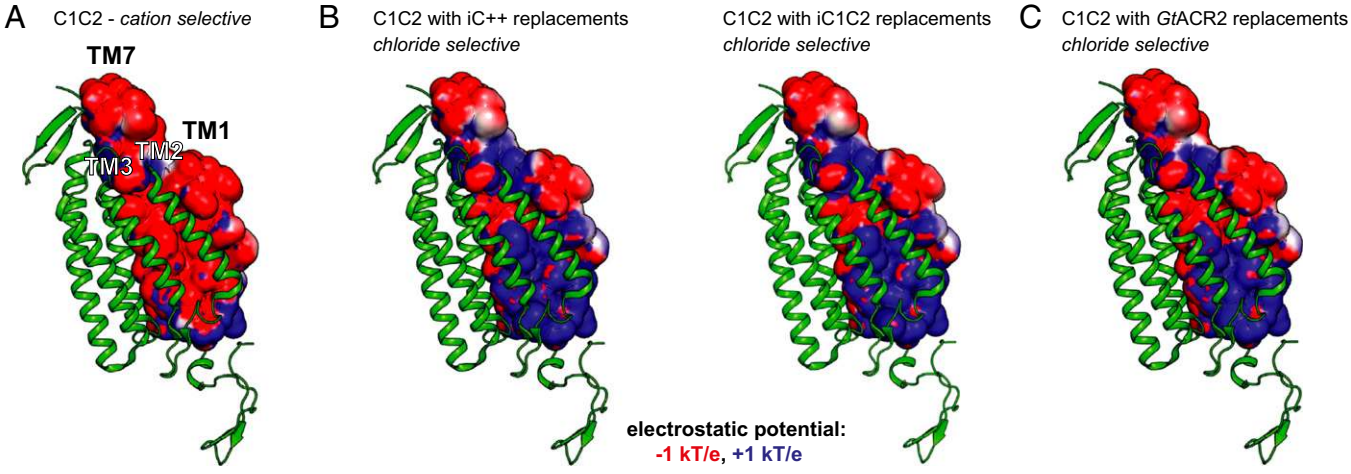

Fig. 2. Model for ion selectivity in channelrhodopsins. (*A*) Structure of the nonselective cation channel C1C2 (Protein Data Bank ID code: 3UG9) (7) with calculated electrostatic potentials of transmembrane helices 1 (TM1) and 7 (TM7), which form the ion-conducting pore together with TM2 and TM3. The electrostatic potential is predominantly negatively charged because of the large number of glutamates facing the pore interior (red: −1 kT/e). Charged groups were considered fully protonated for a simplified first approximation. (*B*) Structures of C1C2 with replacements for iC++ (*Left*) and iC1C2 (*Right*) mutations. The predominantly positive charge of the electrostatic potential of the pore presumably attracts anions and excludes cations (blue: +1 kT/e). (*C*) C1C2 structure with four replacements that are equivalently found in *Gt*ACR2: C1C2-E122S (*Gt*ACR2-S57), C1C2-E136T (*Gt*ACR2-T67), C1C2-E140A (*Gt*ACR2-A71), and C1C2-E162S (*Gt*ACR2-S93). These replacements presumably contribute to the formation of a positively charged, anion-conducting pore.

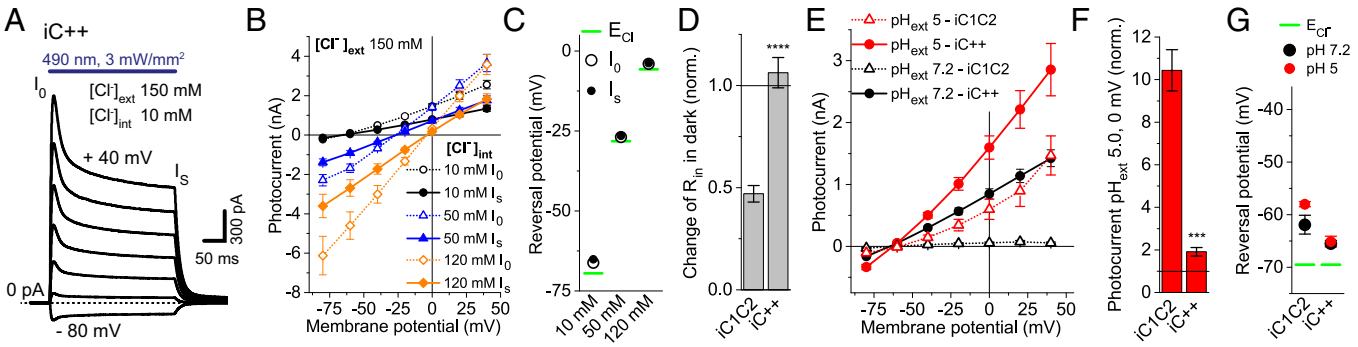

Fig. 3. Biophysical characterization of iC++ in HEK293 cells. (*A*) iC++ photocurrents recorded at membrane potentials from −80 to +40 mV during light application (blue bar). Peak currents (I_0) decay to smaller stationary level (I_S). (*B* and *C*) Amplitudes (*B*) and V_{rev} (*C*) of iC++ peak and stationary currents with 150 mM external ($[Cl^-]_{ext}$) and varying internal $[Cl^-]_{int}$ chloride concentrations. The Nernst equilibrium for chloride (E_{Cl}) is indicated for each condition (green bar). (*D*) Change in R_{in} in iC1C2- and iC++-expressing HEK cells in the dark when $[Cl^-]_{ext}$ was increased from 10 to 150 mM and $[Cl^-]_{int}$ was fixed at 10 mM. Values are normalized to $[Cl^-]_{ext}$ = 10 mM (black line). iC++ does not conduct ions in the dark. (*E*) pH-dependent photocurrents of iC1C2 and iC++ at neutral (black, pH_{ext} 7.2) and acidic (red, pH_{ext} 5.0) external pH values, pH_{int} 7.2. Amplitudes at different pH values were recorded from the same cells. (*F*) Photocurrent at pH_{ext} 5.0/0 mV normalized to values at pH_{ext} 7.2/0 mV (black line). (*G*) V_{rev}s from *E*. ****$P < 0.0001$. Error bars indicate SEM; all values and numbers are listed in *SI Appendix*, Table S2.

that could be encountered in physiological systems, such as aspartate, bicarbonate, and gluconate (*SI Appendix*, Fig. S2).

iC++ Performance Reflects Applied Chloride Gradients. Next, we moved to acute slice recordings to challenge iC++ over a range of physiological chloride gradients within intact tissue. To our knowledge, no previous studies of chloride-conducting channelrhodopsins have varied chloride gradients, but photocurrents and consequently the inhibition of APs depend not only on the expression level in the plasma membranes but also on cytosolic and extracellular chloride concentrations, which vary among cell types, subcellular regions, and developmental stages (12–15). We constructed an adeno-associated viral vector (AAV) carrying the gene encoding iC++ fused to YFP and TS (the membrane-trafficking sequence used for optimizing microbial opsin expression in neurons; ref. 16), all under the control of the CaMKIIα promoter. At 4 wk postinjection into mouse medial prefrontal cortex (mPFC), robust fusion protein expression was observed (Fig. 4*A*). Cell membrane properties were not significantly different from those of control cells expressing only eYFP (*SI Appendix*, Fig. S3).

For physiological relevance to the chloride-driving forces encountered during optogenetic experimentation, photocurrents were measured at the membrane V_{AP} for each cell. As expected from the HEK cell data (Fig. 3 *B* and *C*), channel function (assessed by V_{rev} and photocurrent magnitude) faithfully tracked chloride gradients (Fig. 4 *B* and *C*). To explore the ability of iC++ to inhibit spiking, distinct electrical current-injection protocols (titrated in strength to drive spiking in each individual cell reliably) were tested under different chloride gradients. APs elicited by steady current injections (which elicit more physiological, irregularly spaced spikes than do pulsed current injections) (Fig. 4*D*) were especially susceptible to complete inhibition by iC++ over a broad range of intracellular chloride levels (Fig. 4*E*). When APs were evoked by pulsed current injections, nearly complete spike inhibition was observed even with intracellular chloride elevated beyond the typical physiological range of 4–20 mM, although the inhibition in such cases could be partially overcome with extremely strong (0.8-nA) current injections (*SI Appendix*, Fig. S3).

Next-Generation Step-Function Inhibitory Channelrhodopsin: SwiChR++. One of the most useful properties of channel-type microbial opsins (compared with pumps) for optogenetics is the opportunity to create step-function opsin bistability (17), which allows orders-of-magnitude greater light sensitivity in expressing cells as well as lasting modulation without continuous light delivery (17, 18). Step-function iC1C2 variants, denoted "SwiChR$_{CA}$" and "SwiChR$_{CT}$," were reported previously (17), although the currents were low and efficacy was tested only in vitro. Here, building from the iC++ backbone, we introduced the CA mutation C128A (8), which decelerated iC++ closure ($\tau_{off,fast}$ = 12.1 ms ± 0.4 SEM) by 9,500-fold (resulting in SwiChR++ with $\tau_{off,dark}$ = 115 s ± 9 SEM) (Fig. 5 *A*–*D*). SwiChR++ could be deactivated immediately by red light ($\tau_{off,600nm}$ = 0.15 s ± 0.02 SEM), enabling temporally delimited bistable control over chloride

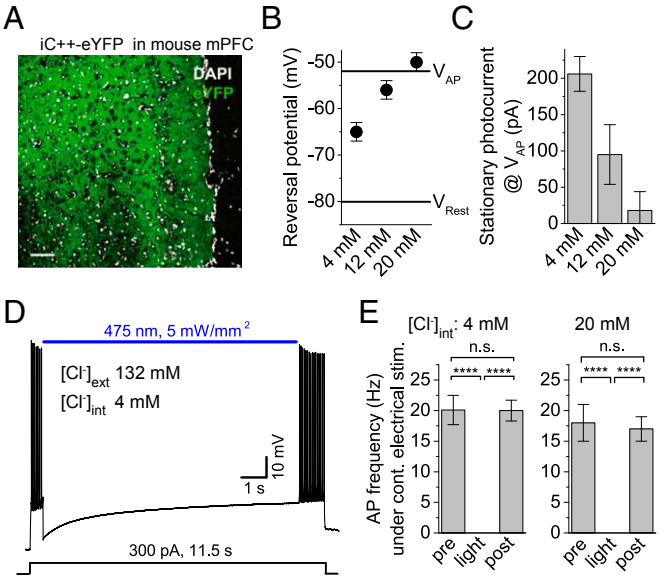

Fig. 4. Chloride-dependent inhibition of pyramidal neurons in mouse mPFC. (*A*) Confocal image of iC++ expression in mPFC 5 wk after virus injection. (Scale bar: 100 μm.) (*B* and *C*) V_{rev}s (*B*) and photocurrents (*C*) of iC++ at the V_{AP} (−52 ± 1 mV) measured for 5 s with light application under varying internal chloride concentrations ($[Cl^-]_{int}$: 4, 12, and 20 mM). Average V_{rest} = –80 mV ± 2. (*D*) Voltage trace of an iC++-expressing neuron showing AP generation by continuous current injections (black bar) and inhibition during 10-s light application (blue bar). (*E*) Spike frequency before (0.5 s), during (10 s), and after (1 s) light application under varying internal chloride concentrations. Continuous current injections were titrated individually to reach the V_{AP}; average: 229 ± 24 pA. n.s.: $P > 0.05$; ****$P < 0.0001$. Error bars indicate SEM; all values and numbers are listed in *SI Appendix*, Table S3.

conductance and neuronal inhibition (Fig. 5 *B* and *D*). SwiChR++ expressed in cultured hippocampal neurons exhibited higher photocurrents and a more negatively shifted V_{rev} than $SwiChR_{CA}$, which resulted in more effective AP inhibition (*SI Appendix*, Fig. S4). SwiChR++ also showed robust in vivo expression and bistable properties over long timescales in mPFC slices, in which V_{rev}, photocurrents, and AP inhibition also depended, as expected, on chloride gradients (Fig. 5 *E*–*G*).

iC++ Inhibition of Neuronal Activity Across Diverse Cell Types and Brain Regions. To examine iC++-mediated inhibition of fast-spiking interneurons, we performed in vivo extracellular recordings within the mPFC of anesthetized PV (parvalbumin):: Cre mice injected with the Cre recombinase-dependent vector AAV8-EF1a::DIO-iC++-EYFP (*SI Appendix*, Fig. S5). Spontaneous activity of PV^+ interneurons was inhibited by light (*SI Appendix*, Fig. S5), with no reduction in the spike frequency of principal (excitatory) mPFC neurons, as expected. To explore the application range of iC++ further, we tested the ability of iC++ to inhibit evoked APs within intact tissue, in this case elicited by the potent neuromodulator oxytocin, which has been shown to depolarize PV^+ interneurons in the hippocampus selectively (19). We injected Cre-dependent AAV carrying iC++ into the hippocampus of PV::Cre mice, observing strong expression >4 wk postinjection (*SI Appendix*, Fig. S6). After confirming iC++ inhibition of electrically evoked APs in these cells (*SI Appendix*, Fig. S6), we applied [Thr^4,Gly^7]-oxytocin (TGOT) to depolarize iC++-expressing PV^+ cells and drive spiking (*SI Appendix*, Fig. S6); light delivery during TGOT application hyperpolarized iC++-expressing cells and abolished all induced firing (*SI Appendix*, Fig. S6).

We broadened the validation to additional cell types, investigating iC++ function in dopaminergic neurons of acute slices from substantia nigra pars compacta and in cultured peripheral dorsal root ganglia neurons. APs were evoked by pulsed current injections (10-ms pulse width). Internal chloride concentrations were kept equal (12 mM) to allow study of inhibition independent of varying chloride gradients. Photocurrent amplitudes were comparable, indicating similar expression levels across all cell types. As before, inputs were titrated to reach the V_{AP} reliably to account for differences between individual cells and cell types. Dopaminergic, dorsal root ganglia, and PV cells all spiked with high reliability even in response to moderate current injection [<360 pA, consistent with relatively depolarized resting membrane potential (V_{rest})], and this spiking was blocked with high efficiency by iC++ (*SI Appendix*, Fig. S6).

Direct Comparison of iC++ and eNpHR3.0 in Vitro: Higher Inhibition Efficiency of iC++. We next carried out a direct comparison with the commonly used chloride pump halorhodopsin engineered from *Natromonas pharaonis* (eNpHR3.0). We delivered AAV8 encoding iC++, eNpHR3.0 (16), or eYFP into the mPFC of mice and assayed expression and activity 4 wk postinjection using patch-clamp electrophysiology in acute slices. The mean R_{in} observed in each condition was similar (*SI Appendix*, Fig. S3). We began by testing inhibition efficiency in response to continuous current injection titrated in a stepwise manner (*SI Appendix*, *SI Methods*) and challenged with 2-s light pulses to drive opsin expression (*SI Appendix*, Fig. S7 *A* and *B*).

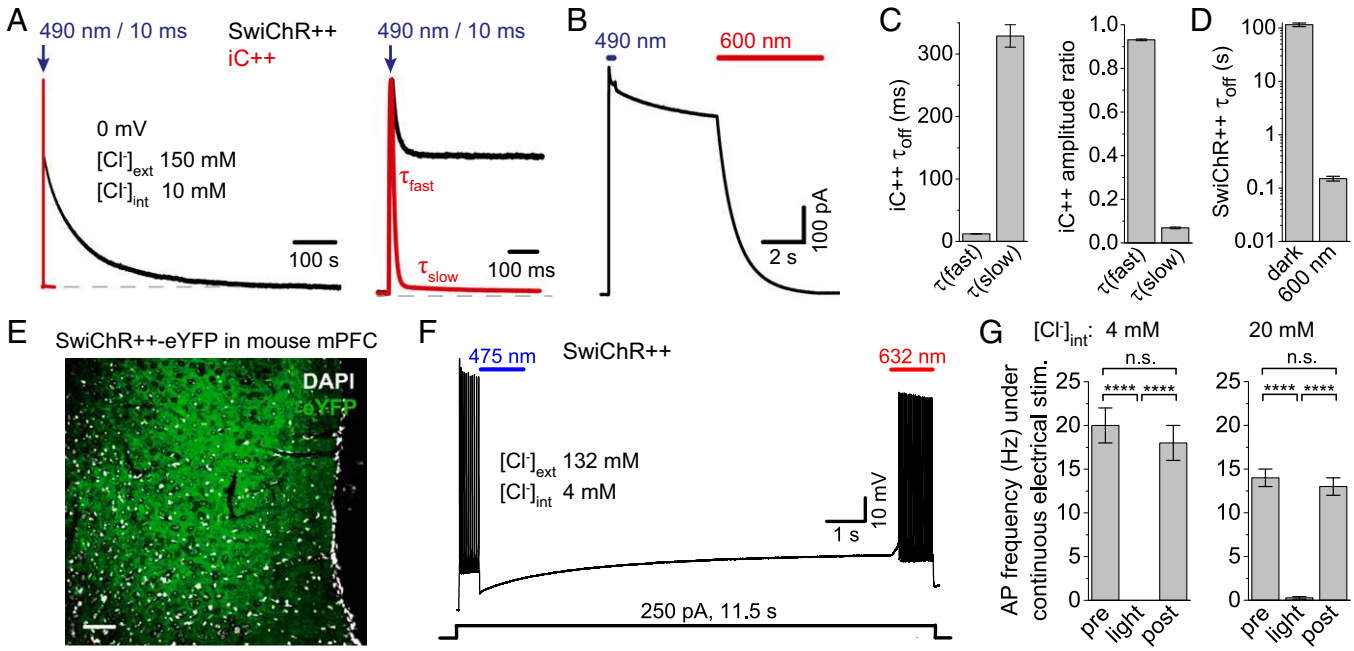

Fig. 5. SwiChR++ characterization in HEK293 cells and neurons from acute mPFC slices. (*A*) Photocurrent traces of iC++ (red) and SwiChR++ (black) showing the time course of the channel closure. (*Left*) Traces were recorded in HEK293 cells at 0 mV in response to brief application of blue light (blue arrow). (*Right*) The same recordings at higher time resolution, depicting the biexponential channel closure of iC++ with a dominant fast component (τ_{fast}) and a slow component (τ_{slow}). (*B*) Photocurrent of SwiChR++ upon the application of blue light (blue bar) and delayed red light (red bar), which accelerates channel deactivation. (*C*, *Left*) Tau values for biexponential channel closure of iC++. (*Right*) Amplitude ratios for the fast (τ_{fast}) and slow (τ_{slow}) components. (*D*) Tau values for the monoexponential channel closure of SwiChR++ in the dark and with the application of light (600 nm). (*E*) Confocal image of SwiChR++ expression in mouse mPFC 5 wk after virus injection. (Scale bar: 100 μm.) (*F*) Voltage trace of an SwiChR++-expressing pyramidal neuron showing APs evoked by continuous current injections (black bar) and inhibition for 10 s upon light application for 1 s (blue bar). Spiking recovers upon red light stimulation (red bar). (*G*) Spike frequency before (0.5 s), during (10 s), and after (2 s) SwiChR activation at varying intracellular chloride concentrations. Input currents were titrated individually to reach the V_{AP}; average: 205 ± 27 pA. n.s.: $P > 0.05$; ****$P < 0.0001$. Error bars indicate SEM; all values and numbers are listed in *SI Appendix*, Table S4.

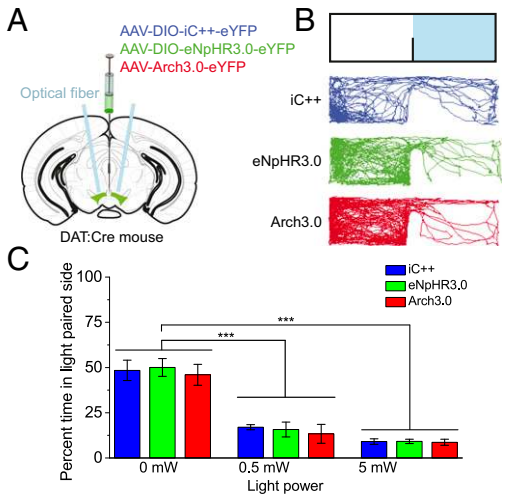

Fig. 6. Place aversion induced by inhibition of dopaminergic VTA neurons in mice. (*A*) An AAV encoding a Cre-dependent opsin (iC++, eNpHR3.0, or eArch3.0 $n = 4$ per group) was injected into the VTA of DAT:Cre mice, and optical fibers were implanted dorsal to this area. (*B*, *Upper*) Schematic of the real-time place-aversion task. Mice were allowed to explore a two-compartment chamber freely. Entry into one compartment triggered continuous illumination (473 nm for iC++; 532 nm for eNpHR3.0 and eArch3.0) as long as the mouse remained in the light-paired compartment. The test was repeated, with distinct contextual cues to minimize generalization, at multiple light intensities. (*Lower*) Representative tracking data from the 5-mW experiment demonstrating robust avoidance of the light-paired compartment. (*C*) Percent time spent in the light-paired compartment at various light intensities. No side preference was observed when the light intensity was 0 mW (light-off control), but at 0.5 mW and 5 mW all groups avoided the light-paired compartment.***$P < 0.005$. Error bars indicate SEM; all values and numbers are listed in *SI Appendix*, Table S5.

Pyramidal cells are especially susceptible to becoming refractory to spiking when large inputs are applied, because of depolarization block. Although pyramidal cells are common targets of optogenetic intervention, this property complicates the assessment of inhibition mediated by opsins when challenged with strong inputs; therefore during titration we did not increase the amplitude of the current input further when the depolarization-blocking potential was reached under light. We found that light delivered to more than 90% of iC++-expressing cells could inhibit any current input tested; conversely, all the eNpHR3.0-expressing cells started to spike at some current amplitude under light (*SI Appendix*, Fig. S7 *D* and *E*). Moreover, eNpHR3.0-expressing cells could inhibit only responses to input currents that were equal to the magnitude of eNpHR3.0 photocurrent; in contrast, iC++-expressing cells were at least seven times more efficient and exhibited a prominent light-induced reduction in R_{in} (*SI Appendix*, Fig. S7*F*). As a result, iC++-expressing cells weakened the impact of current inputs more efficiently than pump-expressing cells, with larger current inputs necessary to evoke APs during illumination (*SI Appendix*, Fig. S7 *G* and *H*). Similar results were observed with pulsed current injection; iC++-expressing cells inhibited a much wider range of input current amplitudes (*SI Appendix*, Fig. S7*I*). The main mechanism of this efficient inhibition from iC++ is likely via shunting inhibition, because the V_{rev} of iC++ lies between the V_{AP} and V_{rest} (revealing that the inhibition is not driven by strong hyperpolarization). Reduction in R_{in} through iC++ activation will reduce excitability, just as seen with endogenous chloride-conducting channels such as $GABA_A$ receptors, providing efficient inhibition via shunting of excitatory inputs (20).

Behavioral Comparison of iC++, eNpHR3.0, and eArch3.0: Real-Time Place-Aversion Test. We next sought to determine if iC++-mediated inhibition would be capable of modifying behavior in freely moving, nonanesthetized animals. We injected AAVs encoding iC++ or, for comparison, eNpHR3.0 or eArch3.0 (21), into the ventral tegmental area (VTA) of DAT::Cre mice for expression in dopaminergic neurons (Fig. 6*A* and *SI Appendix*, Fig. S8. Four weeks later, we optogenetically inhibited VTA dopamine neurons via implanted optical fibers to assess the ability of each opsin to drive behavioral changes in a real-time place-aversion assay. Consistent with prior work (22, 23), we observed robust avoidance of the light-paired compartment at multiple light intensities in all groups (two-way repeated-measures ANOVA, main effect of light power, $F_{2,\ 18} = 64.529$, $P < 0.001$; Holm–Sidak post hoc tests, 0 mW vs. 0.5 or 5 mW, $P < 0.005$) (Fig. 6 *B* and *C*). Under these experimental conditions, each opsin was equally effective in driving real-time place aversion (two-way repeated-measures ANOVA, no effect of group or group × light power interaction, $P > 0.474$). Thus, iC++ is suitable for use in vivo to achieve behaviorally relevant alteration of neural activity.

Inhibition of Memory Retrieval: Potent Behavioral Efficacy of iC++. To test behavioral efficacy further, we used a well-validated assay for memory (involving neuronal allocation to participation in

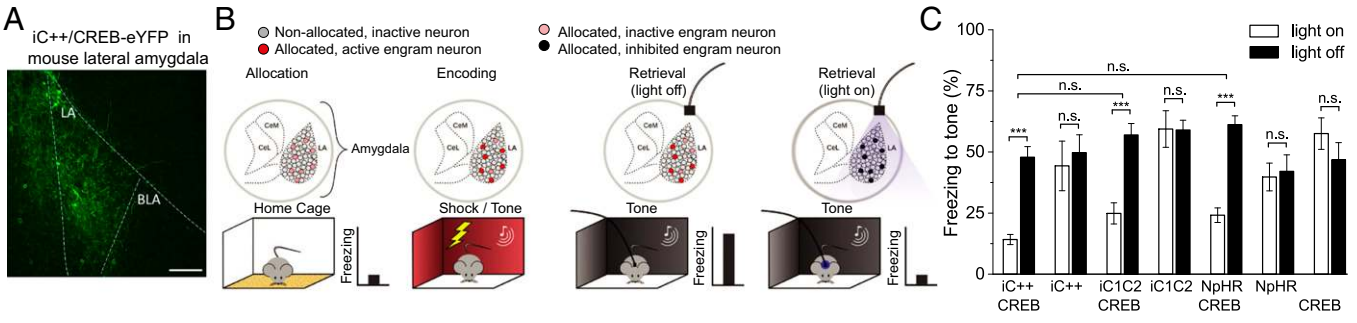

Fig. 7. Using inhibitory channelrhodopsins to silence neurons involved in the engram supporting fear memory. (*A*) Robust, localized transgene expression (green) following microinjection of HSV-CREB/iC++-YFP vector into the LA. (Scale bar: 100 μm.). (*B*) Cartoon of experimental methods used to test the behavioral effects of inhibitory opsins. Mice were microinjected with viral vectors expressing CREB/iC++, CREB/iC1C2, or CREB/eNpHR3.0 into the LA before auditory fear conditioning. Neurons overexpressing CREB are preferentially allocated (red) to the engram supporting the resulting auditory fear memory. Using light to silence these neurons optogenetically results in decreased freezing, indicating impaired memory retrieval. (*C*) Neurons overexpressing CREB before training are preferentially allocated to the engram that supported fear memory. Silencing these neurons using iC++, iC1C2, or eNpHR3.0 reversibly disrupted memory retrieval. Disrupting the activity of the same number of neurons that are not allocated to the fear engram (those not overexpressing CREB) did not impair memory retrieval. n.s.: $P > 0.05$; ***$P < 0.005$. Error bars indicate SEM; all values and numbers are listed in *SI Appendix*, Table S6.

memory engrams). Neurons in the lateral nucleus of the amygdala (LA) are allocated by local circuitry to become part of the engram supporting a discrete cued fear memory (24, 25) in which a tone is paired with a footshock (26–28). Increasing the function of the transcription factor CREB (Ca^{2+}/cAMP response element-binding protein) in individual pyramidal (principal) LA neurons increases the likelihood that the CREB-enhanced neuron will be allocated to a memory engram (24, 25, 29); post-training genetic ablation of LA neurons overexpressing CREB (but not ablation of a comparable number of random LA neurons) impairs memory expression (29).

Optogenetic inhibition of neurons overexpressing CREB was tested for the elicitation of reversible impairment of memory expression (Fig. 7*A*). The short time course of this manipulation allowed comparison of tone-induced freezing behavior in individual mice in the presence and absence of optical inhibition (Fig. 7*B*). We used viral vectors expressing vCREB and iC++, vCREB and iC1C2, or vCREB and eNpHR3.0 (or each inhibitory opsin on its own) to transduce a small portion (~15%) of the LA pyramidal neurons before fear conditioning and tested mice in both the presence and absence of light. Optogenetic inhibition of vCREB neurons using iC++, iC1C2, or eNpHR3.0 significantly reduced tone-induced freezing, whereas silencing a similar number of neurons not overexpressing CREB had no effect [light (on, off) × virus ANOVA yielded a significant interaction, $F_{6,52} = 11.83$, $P < 0.001$] (Fig. 7*C*). Post hoc analyses on the significant interaction showed that light significantly decreased freezing in the vCREB/iC++, vCREB/iC1C2, and vCREB/eNpHR3.0 groups ($P < 0.001$) but not in the iC++, iC1C2, eNpHR3.0, or vCREB-only groups ($P > 0.05$). Of interest, the total freezing scores in the vCREB/iC++ group were even lower than those of the vCREB/iC1C2 group in the light-on condition ($P < 0.05$). However, considering the baseline freezing when light was off, the reduction in freezing was not significantly different among the vCREB/iC++, vCREB/iC1C2, and vCREB/eNpHR3.0 groups ($P > 0.05$). These results support the interpretation that silencing neurons overexpressing CREB at the time of training disrupts memory expression and demonstrate the initial behavioral efficacy of chloride-conducting channelrhodopsin-mediated optogenetic inhibition.

Discussion

Here we describe the engineering of enhanced light-gated chloride channels (iC++ and SwiChR++) by structure-guided modification of ion selectivity, show improved efficiency for optical inhibition of neurons with these proteins, and demonstrate initial behavioral control in freely moving mammals. The earlier iC1C2 channel had shown increased chloride conductivity at low pH values, suggesting that more improvement might be seen under more neutral pH values. We hypothesized that this pH dependency resulted from basic residues in the pore region of iC1C2, with higher probability of protonation under acidic conditions that established favorable electrostatic interactions for chloride ions. By removing more negatively charged residues from the ion-conducting pore and introducing two arginines, we increased the chloride selectivity and also strongly reduced the pH dependency of chloride conductivity. The enhancements comprising iC++ support the model of channelrhodopsin selectivity (8) in which ions are selected primarily by electrostatic interactions between pore and ions. Strikingly, this model is validated further by the recently reported naturally anion-conducting *Gt*ACR channelrhodopsins (10), which contain amino acids at key positions within the ion pore equivalent to those in the earlier designed and reported iC1C2 and in iC++ (11).

In addition to testing the hypothesized mechanisms underlying ion selectivity of channelrhodopsins, we also explored the utility of these tools for neuronal inhibition. We observed that, because of stronger shunting, the chloride channel iC++ inhibited APs more efficiently than the chloride pump eNpHR3.0. Although optogenetic inhibitory pumps display more extreme V_{rev} than the inhibitory channels described here, the pumps can hyperpolarize cells far beyond physiological levels, causing unstable membrane properties (21). This effect can be reduced by lowering light intensity, although this strategy also severely reduces the volume of tissue inhibited by the pumps, which are less light sensitive than channels and, unlike the channels, cannot be converted to a more light-sensitive bistable step-function form. In addition, microbial opsin pump currents will not show the influence of ion gradients reported here for channels; such gradients can differ across cell types, subcellular regions, developmental stages, and pathological states (12–15, 30), even giving rise to excitation under some conditions. For the same reason, iC++ currents will mirror the physiological effects of endogenous open chloride channels more precisely (31, 32).

iC++ and related channels (33) represent a different class of optogenetic tool, which, like any reagent in biology, should be selected based on suitability for preparation and hypothesis. Here we demonstrate the initial use of chloride-conducting channelrhodopsins in the behavior of freely moving animals performing tasks involving the VTA and LA. Beyond this generation of these optogenetic inhibitors that take advantage of physiological ion gradients rather than pumping ions unidirectionally, iC++ and related tools (8–10, 33) also lay the groundwork for a deeper understanding of structure–function relationships involving the light-gated ion conductance pathway of channelrhodopsins. Along with prior work on chloride channel engineering (11, 34–36), this second round of predictive validation of the crystal structure-guided electrostatic model for the channelrhodopsin pore (7, 8, 11) provides basic insight into the operation of the microbial opsin channel proteins.

Materials and Methods

Data analysis and all in vitro methods, including cloning of vectors, virus production, preparation and transfection of cultured neurons and HEK cells, histology, and in vitro electrophysiology, are described in detail in *SI Appendix, SI Methods*. Likewise all methods related to animal subject experimentation, including acute slice preparation and physiology, stereotactic surgery, in vivo electrophysiology, and behavioral tests in freely moving animals, are described in *SI Appendix, SI Methods*. All animal procedures were approved by the Stanford Administrative Panel on Laboratory Animal Care and are in accordance with the National Institutes of Health guidelines for animal research (37).

ACKNOWLEDGMENTS. We thank the entire K.D. laboratory for helpful discussions. K.D. is supported by the National Institute of Mental Health, the Simons Foundation Autism Research Initiative, the National Institute on Drug Abuse, the Defense Advanced Research Projects Agency, the Gatsby Charitable Foundation, and the Wiegers Family Fund. A.B. received support from the German Academic Exchange Service (DAAD) and S.Y.L. received support from the Fidelity Foundation. The M.C. laboratory is supported by the Ragnar Söderbergs Foundation, the Knut and Alice Wallenbergs Foundation, the Swedish Brain Foundation (Hjärnfonden), and the European Research Council. The P.H. laboratory is supported by German Research Foundation (DFG) (SFB1078 B2, FOR1279 SPP1665 to P.H.). The S.A.J. laboratory is supported by the Canadian Institutes of Health Research (CIHR). The S.L.D. laboratory is supported by National Institutes of Health Grant R01NS080954 (to S.L.D. and K.D.). The R.C.M. laboratory is supported by National Institutes of Health Grant 5P50MH086403 (to R.C.M. and K.D.). Both acute and chronic-timescale optogenetic tools for reversible inhibition and other methods reported in this paper are distributed and supported freely (www.optogenetics.org).

1. Zhang F, et al. (2011) The microbial opsin family of optogenetic tools. *Cell* 147(7):1446–1457.
2. Deisseroth K (2014) Circuit dynamics of adaptive and maladaptive behaviour. *Nature* 505(7483):309–317.
3. Li N, Chen TW, Guo ZV, Gerfen CR, Svoboda K (2015) A motor cortex circuit for motor planning and movement. *Nature* 519(7541):51–56.
4. Kravitz AV, et al. (2010) Regulation of parkinsonian motor behaviours by optogenetic control of basal ganglia circuitry. *Nature* 466(7306):622–626.
5. Holland EM, Braun FJ, Nonnengässer C, Harz H, Hegemann P (1996) The nature of rhodopsin-triggered photocurrents in Chlamydomonas. I. Kinetics and influence of divalent ions. *Biophys J* 70(2):924–931.
6. Nagel G, et al. (2002) Channelrhodopsin-1: A light-gated proton channel in green algae. *Science* 296(5577):2395–2398.
7. Kato HE, et al. (2012) Crystal structure of the channelrhodopsin light-gated cation channel. *Nature* 482(7385):369–374.

8. Berndt A, Lee SY, Ramakrishnan C, Deisseroth K (2014) Structure-guided transformation of channelrhodopsin into a light-activated chloride channel. *Science* 344(6182):420–424.
9. Wietek J, et al. (2014) Conversion of channelrhodopsin into a light-gated chloride channel. *Science* 344(6182):409–412.
10. Govorunova EG, Sineshchekov OA, Janz R, Liu X, Spudich JL (2015) NEUROSCIENCE. Natural light-gated anion channels: A family of microbial rhodopsins for advanced optogenetics. *Science* 349(6248):647–650.
11. Berndt A, Deisseroth K (2015) OPTOGENETICS. Expanding the optogenetics toolkit. *Science* 349(6248):590–591.
12. Cossart R, Bernard C, Ben-Ari Y (2005) Multiple facets of GABAergic neurons and synapses: Multiple fates of GABA signalling in epilepsies. *Trends Neurosci* 28(2): 108–115.
13. Glykys J, et al. (2009) Differences in cortical versus subcortical GABAergic signaling: A candidate mechanism of electroclinical uncoupling of neonatal seizures. *Neuron* 63(5):657–672.
14. Tyzio R, et al. (2014) Oxytocin-mediated GABA inhibition during delivery attenuates autism pathogenesis in rodent offspring. *Science* 343(6171):675–679.
15. Wright R, Raimondo JV, Akerman CJ (2011) Spatial and temporal dynamics in the ionic driving force for GABA(A) receptors. *Neural Plast* 2011:728395.
16. Gradinaru V, et al. (2010) Molecular and cellular approaches for diversifying and extending optogenetics. *Cell* 141(1):154–165.
17. Berndt A, Yizhar O, Gunaydin LA, Hegemann P, Deisseroth K (2009) Bi-stable neural state switches. *Nat Neurosci* 12(2):229–234.
18. Yizhar O, et al. (2011) Neocortical excitation/inhibition balance in information processing and social dysfunction. *Nature* 477(7363):171–178.
19. Owen SF, et al. (2013) Oxytocin enhances hippocampal spike transmission by modulating fast-spiking interneurons. *Nature* 500(7463):458–462.
20. Vida I, Bartos M, Jonas P (2006) Shunting inhibition improves robustness of gamma oscillations in hippocampal interneuron networks by homogenizing firing rates. *Neuron* 49(1):107–117.
21. Mattis J, et al. (2012) Principles for applying optogenetic tools derived from direct comparative analysis of microbial opsins. *Nat Methods* 9(2):159–172.
22. Tan KR, et al. (2012) GABA neurons of the VTA drive conditioned place aversion. *Neuron* 73(6):1173–1183.
23. Ilango A, et al. (2014) Similar roles of substantia nigra and ventral tegmental dopamine neurons in reward and aversion. *J Neurosci* 34(3):817–822.
24. Han JH, et al. (2007) Neuronal competition and selection during memory formation. *Science* 316(5823):457–460.
25. Zhou Y, et al. (2009) CREB regulates excitability and the allocation of memory to subsets of neurons in the amygdala. *Nat Neurosci* 12(11):1438–1443.
26. Davis M (1992) The role of the amygdala in fear and anxiety. *Annu Rev Neurosci* 15: 353–375.
27. LeDoux JE (2000) Emotion circuits in the brain. *Annu Rev Neurosci* 23:155–184.
28. Maren S (2003) The amygdala, synaptic plasticity, and fear memory. *Ann N Y Acad Sci* 985:106–113.
29. Han JH, et al. (2009) Selective erasure of a fear memory. *Science* 323(5920):1492–1496.
30. Ferenczi E, Deisseroth K (2012) When the electricity (and the lights) go out: Transient changes in excitability. *Nat Neurosci* 15(8):1058–1060.
31. Huang F, Wong X, Jan LY (2012) International Union of Basic and Clinical Pharmacology. LXXXV: Calcium-activated chloride channels. *Pharmacol Rev* 64(1):1–15.
32. Jentsch TJ, Stein V, Weinreich F, Zdebik AA (2002) Molecular structure and physiological function of chloride channels. *Physiol Rev* 82(2):503–568.
33. Wietek J, et al. (2015) An improved chloride-conducting channelrhodopsin for light-induced inhibition of neuronal activity in vivo. *Sci Rep* 5:14807.
34. Galzi JL, et al. (1992) Mutations in the channel domain of a neuronal nicotinic receptor convert ion selectivity from cationic to anionic. *Nature* 359(6395):500–505.
35. Gunthorpe MJ, Lummis SC (2001) Conversion of the ion selectivity of the 5-HT(3a) receptor from cationic to anionic reveals a conserved feature of the ligand-gated ion channel superfamily. *J Biol Chem* 276(24):10977–10983.
36. Yang H, et al. (2012) TMEM16F forms a Ca2+-activated cation channel required for lipid scrambling in platelets during blood coagulation. *Cell* 151(1):111–122.
37. Committee on Care and Use of Laboratory Animals (1996) *Guide for the Care and Use of Laboratory Animals* (Natl Inst Health, Bethesda), DHHS Publ No (NIH) 85-23.